

X-ray AGN in the XMM-LSS galaxy clusters: no evidence of AGN suppression.

E. Koulouridis¹, M. Plionis^{2,3,1}, O. Melnyk^{4,5}, A. Elyiv^{4,6,7}, I. Georgantopoulos¹, N. Clerc⁸, J. Surdej⁴, L. Chiappetti⁹,
M. Pierre¹⁰

¹ Institute for Astronomy & Astrophysics, Space Applications & Remote Sensing, National Observatory of Athens, Palaia Penteli 15236, Athens, Greece.

² Physics Department of Aristotle University of Thessaloniki, University Campus, 54124, Thessaloniki, Greece

³ Instituto Nacional de Astrofísica Óptica y Electrónica, Puebla, C.P. 72840, México.

⁴ Institut d'Astrophysique et de Géophysique, Université de Liège, 4000 Liège, Belgium

⁵ Astronomical Observatory, Taras Shevchenko National University of Kyiv, 3 Observatorna St., 04053 Kyiv, Ukraine

⁶ Dipartimento di Fisica e Astronomia, Università di Bologna, Viale Berti Pichat 6/2, I-40127 Bologna, Italy

⁷ Main Astronomical Observatory, Academy of Sciences of Ukraine, 27 Akademika Zabolotnoho St., 03680 Kyiv, Ukraine

⁸ Max-Planck-Institute for Extraterrestrial Physics, Giessenbachstrasse 1, 85748, Garching, Germany

⁹ INAF, IASF Milano, via Bassini 15, I-20133 Milano, Italy

¹⁰ Service d'Astrophysique, AIM, CEA Saclay, F-91191 Gif sur Yvette.

November 21, 2021

ABSTRACT

We present a study of the overdensity of X-ray-selected active galactic nuclei (AGN) in 33 galaxy clusters in the XMM-LSS field (The XMM-Newton Large Scale Structure Survey), up to redshift $z = 1.05$ and further divided into a lower ($0.14 \leq z \leq 0.35$) and a higher redshift ($0.43 \leq z \leq 1.05$) subsample. Previous studies have shown that the presence of X-ray-selected AGN in rich galaxy clusters is suppressed, since their number is significantly lower than what is expected from the high galaxy overdensities in the area. In the current study we have investigated the occurrence of X-ray-selected AGN in low ($\langle L_x, bol \rangle = 2.7 \times 10^{43}$ erg/s) and moderate ($\langle L_x, bol \rangle = 2.4 \times 10^{44}$ erg/s) X-ray luminosity galaxy clusters in an attempt to trace back the relation between high-density environments and nuclear activity. Owing to the wide contiguous XMM-LSS survey area, we were able to extend the study to the cluster outskirts. We therefore determined the projected overdensity of X-ray point-like sources around each cluster out to $6r_{500}$ radius, within $\delta r_{500} = 1$ annulus, with respect to the field expectations based on the X-ray source $\log N - \log S$ of the XMM-LSS field. To provide robust statistical results we also conducted a consistent stacking analysis separately for the two z ranges. We investigated whether the observed X-ray overdensities are to be expected thanks to the obvious enhancement of galaxy numbers in the cluster environment by also estimating the corresponding optical galaxy overdensities, and we assessed the possible enhancement or suppression of AGN activity in clusters.

We find a positive X-ray projected overdensity in both redshift ranges at the first radial bin, which however has the same amplitude as that of optical galaxies. Therefore, no suppression (or enhancement) of X-ray AGN activity with respect to the field is found, in sharp contrast to previous results based on rich galaxy clusters, implying that the mechanisms responsible for the suppression are not as effective in lower density environments. After a drop to roughly the background level between 2 and $3r_{500}$, the X-ray overdensity exhibits a rise at larger radii, significantly greater than the corresponding optical overdensity. The radial distance of this overdensity “bump”, corresponding to $\sim 1.5 - 3$ Mpc, depends on the richness of the clusters, as well as on the overall X-ray overdensity profile. Finally, using the redshift information, photometric or spectroscopic, of the optical counterparts, we derive the spatial overdensity profile of the clusters. We find that the agreement between X-ray and optical overdensities in the first radial bin is also suggested in the 3-dimensional analysis. However, we argue that the X-ray overdensity “bump” at larger radial distance is at least partially a result of flux boosting by gravitational lensing of background QSOs, confirming previous results. For high-redshift clusters the enhancement of X-ray AGN activity in their outskirts appears to be intrinsic. We argue that a spatial analysis is crucial for disentangling irrelevant phenomena affecting the projected analysis, but we are still not able to report statistically significant results on the spatial overdensity of AGN in clusters or their outskirts because we lack the necessary numbers.

Key words. galaxies: active – galaxies: Clusters: general – X-rays: galaxies: clusters – galaxies: interactions – galaxies: evolution – cosmology: large scale structure of Universe

1. Introduction

As one of the most powerful extragalactic phenomena, active galactic nuclei (AGN) are a valuable tool in the study of the universe, since they can be used as cosmological probes, provide answers to various problems of galaxy evolution, and shed light on the innermost regions of galaxies, where the super massive black hole resides and highly energetic processes take place. However, the triggering mechanism of the omnipresent, but not

always active, black hole is still elusive. Although major merging of gas-rich galaxies seems to be a highly probable mechanism for the triggering of nuclear activity (e.g., Sanders et al. 1988; Barnes & Hernquist 1991; Hopkins et al. 2006), recent studies of the morphology of AGN hosts find no evidence of a major merging-AGN connection (e.g., Cisternas et al. 2011; Kocevski et al. 2012). On the other hand, minor merging and interactions are still strongly disputed, while secular evolution

also seems able to feed the central engine since many AGN are found to be isolated and undisturbed (e.g., Hopkins & Hernquist 2006; Cisternas et al. 2011; Kocevski et al. 2012). Therefore, the effect of the environment on the activity of the nucleus and vice versa is still fairly undetermined, but nevertheless crucial. Galaxy clusters represent the one end of the density spectrum in our universe, and as such it is an ideal place to investigate the effects of dense environment in the triggering of AGN, especially since an excessive number of X-ray point-like sources are undoubtedly found there (e.g., Cappi et al. 2001; Molnar et al. 2002; Johnson et al. 2003; D’Elia et al. 2004; Gilmour et al. 2009). Specifically, for the XMM-LSS field investigated in the current study, Melnyk et al. (2013) have found that 60% of X-ray-selected AGN reside in the overdense regions of group-like environment.

Theoretically the feeding of the black hole can only be achieved by means of a non-axisymmetric perturbation that induces mass inflow. This kind of perturbation can be provided by interactions and merging between two galaxies, and the result of the inflow is the feeding of the black hole and activation of the AGN phase (e.g., Umemura 1998; Kawakatu et al. 2006; Koulouridis et al. 2006a, 2006b, 2013, Ellison et al. 2011; Silverman et al. 2011; Villforth et al. 2012; Hopkins & Quataert 2011). Thus, the cluster environment, where the concentration of galaxies is very high relative to the field, would also seem favorable to AGN. However, the rather extreme conditions within the gravitational potential of a galaxy cluster can work in the opposite direction as well. Ram pressure from the inter cluster medium (henceforth ICM) able to strip/evaporate the cold gas reservoir of galaxies (Gunn & Gott 1972; Cowie & Songaila 1977; Giovanelli et al. 1985) can strongly affect the feeding of the AGN. Nevertheless, other studies have argued that ram pressure stripping cannot be as effective in transforming blue sequence galaxies to red (e.g., Larson et al. 1980; Balogh et al. 2000, 2002; Bekki et al. 2002; van den Bosch et al. 2008; Wetzel et al. 2012), especially in lower density clusters where other processes should take place as well. Large velocity dispersion of galaxies within clusters could also prevent the effective interactions (Aarseth & Fall 1980), particularly mergers, while the fast “grazing” bypassing galaxies may also cause gas stripping by “harassment” (e.g., Natarajan et al. 2002, Cypriano et al. 2006). However, the efficiency of this phenomenon has once more been questioned (e.g., Giovanardi et al. 1983). A combination of the above mechanisms, in addition to the possible prevention of accretion of halo mass into cluster galaxies (“strangulation”; e.g., Larson et al. 1980; Bekki et al. 2002; Tanaka et al. 2004) may, in fact, suppress the AGN activity in clusters despite the number of potentially merging and interactive galaxies.

When using only optical data, the results seem to remain inconclusive. Early studies reported that AGN are less frequent in galaxy clusters than in the field (Osterbrock 1960; Gisler 1978; Dressler, Thompson & Schectman 1985) and recent large-area surveys support this suggestion (Kauffmann et al. 2004; Popesso & Biviano 2006; von der Linden et al. 2010; Pimblet et al. 2013). Other studies, however, have found no differences between clusters and field (e.g., Miller et al. 2003), at least when selecting the weak AGN (e.g., Martini et al. 2002; Best et al. 2005; Martini et al. 2006; Haggard et al. 2010). We should note here that considering only the optical wavelengths is not the optimal way of finding AGN since they suffer greatly from absorption. Especially if gas depletion is at play and low accretion rates are expected, then most of the spectral signatures of the AGN could be “buried” in the host galaxy.

Radio-loud AGN on the other hand, seem to be more clustered than any other type of galaxy (Hart, Stocke & Hallman 2009) and are often associated with BCGs (brightest cluster galaxies)(e.g., Best 2004; Best et al. 2007). In addition, the fraction of X-ray AGN in BCGs is higher than in other cluster galaxies (e.g., Hlavacek-Larrondo et al. 2013, and references therein). These findings can be attributed to hot gas accretion from the hot X-ray cluster halo, although gas from any other source fueling the black hole at low accretion rates would also have the same effect. If the hot gas accretion is a possible fueling mechanism for the X-ray AGN, as well, then we should expect them to reside primarily within clusters.

Undoubtedly, the best way to detect active galaxies is through X-ray observations (e.g., Brandt & Alexander 2010). However, during the previous decade, only a small fraction of X-ray point-like sources in clusters had positive confirmation as true cluster members (see Martini et al. 2002; Davis et al. 2003; Finoguenov et al. 2004; Arnold et al. 2009), leaving the question of whether the positive X-ray overdensities found in galaxy clusters represent enhancement or suppression of the nuclear activity unanswered. More recent studies, however, report more conclusive results by comparing X-ray to optical data. Koulouridis & Plionis (2010) demonstrate the significant suppression of X-ray-selected AGN in 16 rich Abell clusters (Abell et al. 1958) by comparing the X-ray point source overdensity to the optical galaxy overdensity. Ehlert et al. (2013; 2014) argue that the X-ray AGN fraction in the central regions of 42 of the most massive clusters known to date is about three times lower than the field value using the same technique. More importantly, after having complete spectroscopy for their X-ray point source sample, Haines et al. (2012) argue that X-ray AGN found in massive clusters are an infalling population, which is “extinguished” later, and confirm the suppression in rich clusters. On the other hand, Martini et al. (2013) argue that this trend is not confirmed for a sample of high-redshift clusters ($1.0 < z < 1.5$), where the presence of luminous X-ray AGN ($L_{(0.5-2 \text{ keV})} > 10^{43} \text{ erg/s}$) is consistent with the field. We note, however, that the high-redshift regime studied and the large AGN photometric redshift uncertainties ($\sigma_z = 0.12(1+z)$, double that of normal galaxies) introduce some level of uncertainty to the results. Nevertheless, they agree with findings from the DEEP2 Redshift Survey¹ that show that only below $z=1.3$ does the fraction of blue galaxies in groups drop rapidly and become constant below $z=1$ (Gerke et al. 2007), while the red fraction correlates weakly with overdensity above $z=1.3$ (Cooper et al. 2007). In the present study we only deal with clusters $z < 1.05$, where the cluster’s population is dominated by early type red galaxies. Finally, we should also mention that an indirect way to address the issue is by X-ray clustering analyses, but still their results also remain inconclusive (see relevant discussion in Haines et al. 2012 §5.2).

Considering the above, there is still the need to clarify the influence of the environment on the AGN phenomenon. And while the majority of the above studies are dealing with the most massive and rich clusters, the population of moderate-to-poor clusters is still overlooked.² If the reason for the deficiency of

¹ <http://deep.ps.uci.edu/>

² We should note that the categorization of galaxy clusters to different richness classes is not explicit, and it is safer to be used statistically. Nevertheless, the relation between mass and X-ray properties is well studied (e.g., Edge & Stewart 1991a, b; Finoguenov, Reiprich & Bohringer, 2001) and, also considering more recent studies of X-ray luminous clusters (e.g., Ebeling et al. 2010), we can infer that massive clusters have X-ray luminosities higher than $\sim 5 \times 10^{44} \text{ erg/s}$ and temperatures higher than $kT > 5 \text{ keV}$.

X-ray AGN in rich clusters is the strong gravitational potential, which provides the necessary conditions for the suppression (whichever these may be: gas stripping, strangulation, tidal stripping, evaporation, high velocity dispersion, etc.), one would expect the AGN presence to rise in shallower gravitational potentials. A similar relation between the strength of the gravitational potential and star formation quenching (Popesso et al. 2012) supports the above expectation (see also Wetzel et al. 2012). Another issue is the radial extent of the search for X-ray AGN around clusters. An enhancement of AGN activity is observed far from the cluster’s center (e.g., Fassbender et al. 2012), and it could be due to an infalling population (Haines et al. 2012) coming from the “outskirts” of the clusters where the concentration of galaxies is still high. The question is where should we place the “outskirts” and to what extent. Most studies could not reach farther than a $2r_{500}$ radius, although the overdensity profile of optical galaxies remains higher than the field level even beyond that radius (e.g., Ehlert et al. 2013). Finally, what is also overlooked is the background overdensity of X-ray sources in the area of clusters. In Koulouridis et al. (2010), we used SDSS (Sloan Digital Sky Survey) optical data for all the detected X-ray point-like sources within a 1 Mpc radius, and argue that their positive overdensity values were associated with background QSOs rather than cluster members. A possible cause is the gravitational lensing of background sources, which is unimportant when compared to the large number of optical galaxies in clusters but can become very important for X-ray sources and affect the assessment of their clustering.

In the current study, our aim is to investigate the AGN phenomenon in the environment of moderate and poor clusters located in the XMM-LSS contiguous field of 11.1 deg^2 . We identify all possible X-ray AGN candidates, which we define as sources with $L_{(0.5-2 \text{ keV})} > 10^{42} \text{ erg/s}$ at the redshift of the cluster, and compare their overdensity in the area of the clusters to the respective overdensity of optical galaxies, available by the CFHT legacy survey. Such a large contiguous area gives us the unique opportunity not only to use a large cluster sample but also to extend our search for X-ray AGNs around clusters at great distances, reaching homogeneously up to a $6r_{500}$ radius. In addition, we make use of photometric redshift data calculated specifically for X-ray-selected AGN hosts, in an attempt to assess the true number of X-ray AGNs in our clusters and clarify the effect of the excessive overdensity of background X-ray sources (e.g., Koulouridis & Plionis 2010).

We describe our samples and methodology in §2, while our results and conclusions are presented in §3 and §4, respectively. Throughout this paper we use $H_0 = 72 \text{ km/s/Mpc}$, $\Omega_m = 0.27$, and $\Omega_\Lambda = 0.73$.

2. Sample selection & methodology

2.1. The XMM-LSS

The XMM-LSS field is part of the XXL survey, which is the largest international XMM project approved to date (>6Msec), surveying two 25 deg^2 fields at a depth of $\sim 3 \times 10^{-15} \text{ erg cm}^{-2} \text{ s}^{-1}$ in the $[0.5-2] \text{ keV}$ band. It occupies an area of 11.1 deg^2 and is located at high galactic latitudes ($2^h 14^m < \text{ra} < 2^h 30^m$; $-6^{\circ} 25' < \text{dec} < -2^{\circ} 35'$, J2000.0, see also Fig. 1). It is contiguous, consists of 94 pointings with effective exposures from 10 ks to 40 ks and contains the Subaru X-ray Deep Survey (SXDS; Ueda et al. 2008) that covers 1.14 deg^2 of the area³. The XMM-

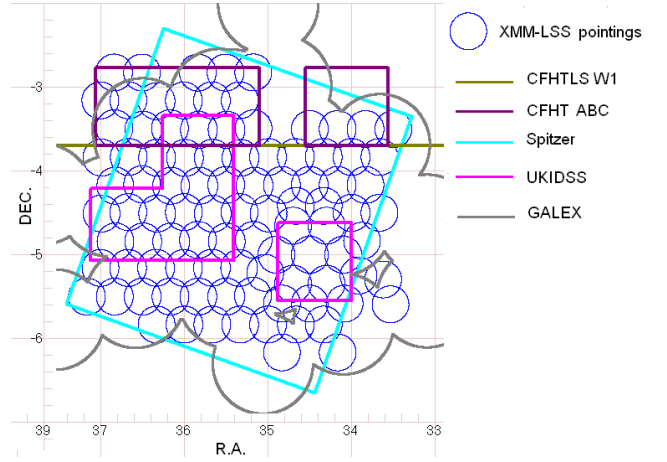


Fig. 1. Multiwavelength coverage of the XMM-LSS field. Colored borders demarcate the regions covered by The Canada-France-Hawaii Telescope Legacy Survey (CFHTLS W1, below the green horizontal line), the Canada-France-Hawaii Telescope (CFHT) ABC supplementary pointings, Spitzer Space Telescope (SST), the UKIRT Infrared Deep Sky Survey (or UKIDSS) and The Galaxy Evolution Explorer (GALEX).

LSS full-exposure field contains 6342 sources^2 , 5737 of them detected in the soft $[0.5-2] \text{ keV}$ band down to a detection likelihood of 15 ($\sim 1\%$ spurious, see Pacaud et al. (2006) for more details about the source detection and the statistics). The effective flux limit in the soft band is $F_{(0.5-2 \text{ keV})} = 3 \times 10^{-15} \text{ erg s}^{-1} \text{ cm}^{-2}$, which corresponds to 50% sky coverage according to the effective area curves of Elyiv et al. (2012). The large majority of the X-ray sources is point-like ($N = 5570$), which are mainly AGN since the expected stellar contamination is near 3%. twenty-eight percent of the sources are excluded mostly due to the lack of sufficient photometry bands (<4), lack of counterpart ($\sim 4\%$), and double-peaked photometric redshift solution.

We therefore used 72% of the full sample, of which 17% had spectroscopic redshifts (see §2.6), although the respective completeness around our clusters is $\sim 81\%$, and spectroscopic redshifts are available for $\sim 24\%$ of the total (see §3.3), respectively. More details about the catalog’s sensitivity, the effective area curve, and the $\log N - \log S$ can be found in Elyiv et al. (2012) and in the multiwavelength catalog description paper by Chiappetti et al. (2013). We note that the soft-band $\log N - \log S$ used in the current study, calculated by Elyiv et al. (2012), is lower than those of the 2XMM (Ebrero et al. 2009) and COSMOS (Capelluti et al. 2007) surveys (with deviations not exceeding the $2 - 3\sigma$ Poisson level), but in excellent agreement with those of the XMM Medium Deep Survey (XMDS, Chiappetti et al. 2005).

2.2. The cluster sample

The clusters of galaxies used in this study were selected to meet the following conditions:

1. They belong to the list of unambiguously confirmed C1 clusters of the XMM-LSS field (Adami et al. 2011; Pacaud et al. 2006; Pierre et al. 2006).
2. They are not located near the edges of the XMM-LSS field, to ensure the complete detection of all point-like sources within the radii of interest.

³ The data are available in the Milan DB in the 2XLSSd and 2XLSSOPTd tables. See Chiappetti et al. (2013) for details.

- They belong to the redshift range $z < 1.05$. The upper limit is set at a reasonable redshift above which the lower X-ray source luminosity that corresponds to the lower flux limit is becoming very high (the lower flux limit is set at a certain value; see next paragraph).

For all clusters that meet the above criteria, we list in Tables 1 and 2 (from Clerc et al. 2014, in prep.): the temperatures and X-ray luminosities (giving an estimate of their richness and of the depth of the gravitational potential of the cluster), and the r_{500} radius calculated by fitting a beta model to the extended emission (see also Pacaud et al. 2007). The positions of all the clusters and their corresponding $4r_{500}$ ($5r_{500}$ for the high- z sample) radius are overplotted on the XMM-LSS X-ray map in Fig. 2. In the full XMM-LSS sample used in this work, the median number of photons used for the X-ray spectral fit is 350 (in [0.5–2] keV), and the median statistical error on the temperatures is 15%. Regarding the temperatures, the interested reader can refer to Willis et al. (2006) (in their appendix), where they simulated various clusters and applied a similar X-ray spectral measurement procedure to derive the temperature uncertainties.

We limited our analysis to sources above a flux limit of $3 \times 10^{-15} \text{ erg s}^{-1} \text{ cm}^{-2}$, since at lower fluxes, sources were scarcely detected in the XMM-LSS survey and thus the resulting $\log N - \log S$ bears large uncertainties in this flux regime.

To have homogeneous samples in X-ray luminosity, as well as to study possible evolutionary effects, we divided the 33 clusters into two subsamples, a lower and higher redshift sample. The low- z sample ($0.14 \leq z \leq 0.35$) consists of 19 clusters with average X-ray luminosity $\langle L_x, \text{bol} \rangle = 2.7 \times 10^{43} \text{ erg/s}$ and average temperature $\langle kT \rangle = 2.0 \text{ keV}$, while the high- z sample ($0.43 \leq z \leq 1.05$) of 14 clusters with average X-ray luminosity $\langle L_x, \text{bol} \rangle = 2.4 \times 10^{44} \text{ erg/s}$ and average temperature $\langle kT \rangle = 3.1 \text{ keV}$. Based on the X-ray luminosity and temperature of our clusters, we have no rich clusters in our samples (Alshino et al. 2010), with the exception of XLSSC 006, while the low- z sample mostly consists of poor systems and the high- z mostly of intermediate systems. We imposed a limiting X-ray luminosity of 10^{42} erg/s for our X-ray sources, in order to securely select X-ray AGN. Therefore, the corresponding X-ray flux limit is such that for the low- z sample, the rest-frame luminosity limit is always $L_{(0.5-2 \text{ keV})} = 10^{42} \text{ erg/s}$, which means that we are complete in X-ray luminosity. However, this is not the case for the high- z sample. Especially for clusters above $z \sim 0.95$ the X-ray luminosity limit is $L_{(0.5-2 \text{ keV})} = 1.7 \times 10^{42} \text{ erg s}^{-1}$ and reaches to $L_{(0.5-2 \text{ keV})} = 1.4 \times 10^{43} \text{ erg s}^{-1}$ for the two clusters at redshift $z \sim 1$ (see Table 2).

2.3. X-ray source overdensity

The X-ray AGN overdensity, in a given area, is estimated according to

$$\Delta_x = \frac{N_x - N_{\text{exp}}}{N_{\text{exp}}}$$

where N_x the number of X-ray point-like sources detected in the area and N_{exp} is the expected number according to the $\log N - \log S$ within the same area. To calculate the value of N_x , we identify all point-like sources located within five (six for the high- z clusters) radial annuli between n and $(n+1)r_{500}$, where $n = 0, 1, 2, \dots, 5$. We consider only the sources with X-ray fluxes $f_{(0.5-2 \text{ keV})} > f_{\text{lim}}$, where f_{lim} is the specific value of the flux for which the AGN X-ray luminosity at the distance of any cluster is $L_{(0.5-2 \text{ keV})} = 10^{42} \text{ erg/s}$. The large contiguous area of

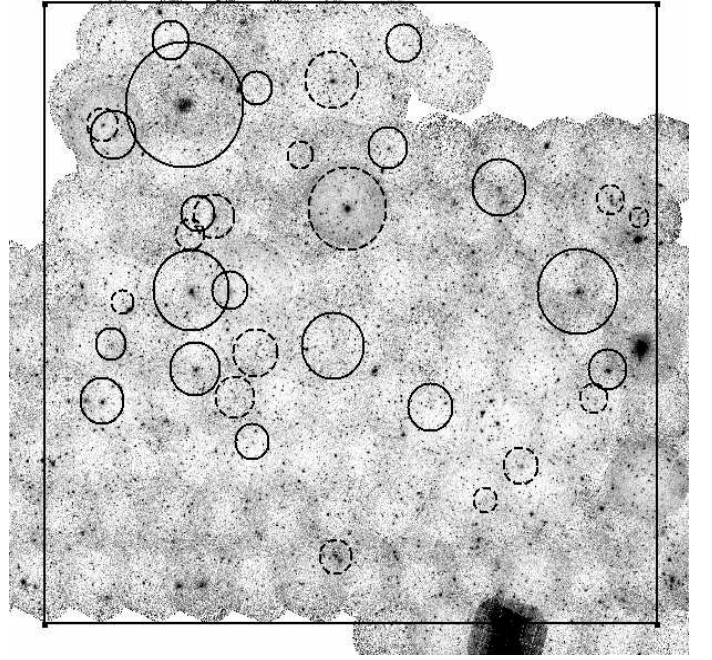


Fig. 2. Position and $4r_{500}$ ($5r_{500}$) radius of the current study's low-redshift (high-redshift - dashed circles) clusters in the XMM-LSS region (square).

the XMM-LSS survey allows us to expand our search for X-ray AGN activity at large radii from the cluster cores and gives us the opportunity to explore possible evolutionary trends of nuclear activity as galaxies enter the cluster's gravitational potential from their outskirts.

Because of the cluster's diffuse X-ray emission, in most cases we may not be able to sufficiently resolve the central region and could possibly fail to detect X-ray AGN in that area. Thus, we choose to exclude a fraction of the first r_{500} annulus from each cluster to avoid introducing a possible bias into our results. However, the area that has to be excluded depends on the strength of the extended emission, as well as on the imposed lower flux limit of the X-ray sources we wish to detect, and therefore it varies from cluster to cluster. In Koulouridis et al. (2010), we excluded the regions with $r < r_{\text{core}}$, where r_{core} was found by fitting a β model to the extended X-ray emission. For the current analysis, we inspected all clusters visually and chose to exclude the inner $0.5 \times r_{500}$ homogeneously from all clusters. We found that the extracted area eliminates the problem of diffuse X-ray emission in all clusters and furthermore allows us to do a meaningful comparison and stacking of the first annuli of different clusters.

To calculate the expected number N_{exp} of X-ray sources in the field, we followed the procedure described below, considering each time the same area of the detector and the same characteristics of the actual observation:

- From the $\log N - \log S$ of the XMM-LSS survey (see Elyiv et al. 2012 for a more detailed analysis), we derive the total number (N_f) of expected sources in the area per flux bin.
- We consider $1000 \times N_f$ sources with random fluxes within the flux range of each bin and random position within the area of interest.
- We derive the probability P_i that the source N_{fi} is actually detected in the specific area of the detector. The probability is

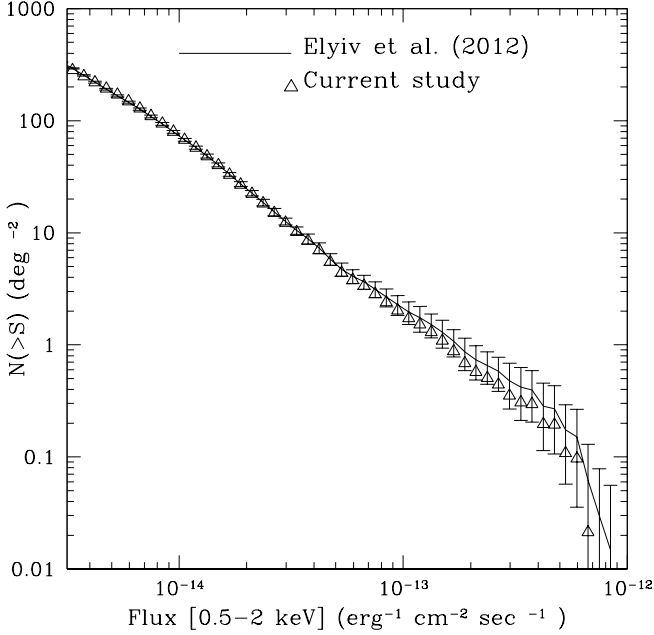


Fig. 3. $\log N - \log S$ distribution in the soft band for the whole XMM-LSS sample (line). The triangles denote the test values derived from random sources in the area of 10 galaxy clusters in the current study. Errorbars denote the 1σ Poissonian uncertainty of the Elyiv et al. (2012) points.

a function of the off-axis position (vignetting), background, and exposure time.

4. We calculate the sum: $\sum_{j=n}^{53} \sum_{i=1}^{1000N_j} N_{fi} \times P_i / 1000$, which gives us the total number, N_{exp} , of expected X-ray sources that have fluxes above the respective value of the n^{th} bin of the $\log N - \log S$, where the total number of bins is 53.

To validate the above procedure, we randomly picked ten clusters with 200000 random sources, and we attempted to reproduce the $\log N - \log S$ by using the area curve of the XMM-LSS field. To this end, we binned the sources in the same flux bins and then divided the number of sources in each bin with the fraction of the XMM-LSS area where we could actually detect them. We indeed recover the input $\log N - \log S$ with great accuracy as we can see in Fig. 3. The apparent deficiency of sources in the flux bins above $10^{-13} \text{ erg s}^{-1} \text{ cm}^{-2}$, which is due to the rarity of these sources in the full XMM-LSS field, is very small (< 0.2 sources/deg²), well within the errors, and not important to the current analysis.

2.4. Optical galaxy overdensity

For calculating the optical overdensity in each XMM-LSS cluster, we use the i -band magnitude of the CFHTLS, which is complete up to $m_i \sim 24$, a crucial feature for our high redshift clusters.

As for the X-ray overdensity, the relevant expression is

$$\Delta_o = \frac{N_o - N_{o,\text{exp}}}{N_{o,\text{exp}}},$$

where N_o is the number of optical sources found in the area and $N_{o,\text{exp}}$ the expected background number within the same

area. For the calculation of the galaxy density, within the regions previously defined for the X-ray analysis, we include only those sources with i -band magnitude that satisfy the criterion $m_i^* - 1 < m_i < m_i^* + 1$, where m_i^* is the apparent i -band magnitude that corresponds to the break of the luminosity function at the redshift of each cluster. We should note that we have also conducted the same analysis using $m_i^* - 0.5 < m_i < m_i^* + 0.5$, but the results are exactly the same. For calculating m_i^* , we used the K-correction values derived specifically for the CFHT i -band magnitudes by Ramos et al. (2011) for elliptical galaxies, since most of the cluster's galaxies are expected to be ellipticals. The background galaxy density is calculated from a 2 deg^2 field within the XMM-LSS area.

We should note here that the comparison of the optical galaxy overdensity to the X-ray AGN overdensity should not be considered explicit but rather instructive. Although by using the $L_{(0.5-2 \text{ keV})} > 10^{42} \text{ erg/s}$ criterion, all X-ray sources at the cluster rest frame are potential AGN, and on the other hand, by using the $m_i^* - 1 < m_i < m_i^* + 1$ criterion we choose the bright cluster galaxies that could potentially host the AGN, there is no way of knowing if we are exactly probing the same population of galaxies.

However, the method that we are using in the present study and which has been used in various others (e.g., Martini et al. 2013; Ehlert et al. 2014) over the past years with small variations, can give us valuable information about the presence of AGN in clusters. Finally, as an extra step, we also use the available photometric and spectroscopic redshift data, in an attempt to constrain the true overdensities of X-ray AGN better, since there is evidence that their overdensities, within a ~ 1 Mpc radius around rich clusters, may be affected by gravitational lensing (Koulouridis et al. 2010).

The use of the CFHTLS survey has two caveats related to our current study: it has “holes” with no available data as the result of star masking, and more importantly it does not cover the whole XMM-LSS field. The former may cause the underestimation of some cluster's optical overdensities, so we proceeded with corrections when necessary and we verified that, overall, the “holes” do not affect our statistical results based on stacking. On the other hand, the region outside the CFHT Legacy Survey is instead covered by the CFHT ABC supplementary pointings. However, the available optical CFHT photometric bands in these fields are less than in the CFHTLS (one to three instead of five bands), resulting in less reliable photometric redshifts of the X-ray point source counterparts (calculated using only four to six bands depending on the Spitzer and UKIDSS coverage, see Fig.1). More importantly, there is no i band, which is essential for our projected analysis, and no photometric redshifts of the optical galaxies, which are necessary for our spatial analysis. Thus, when the ABC fields are included in our analysis, the results are given separately and are treated with caution.

2.5. Weighting and stacking

To have more robust results, we also stack, at rest frame, the respective annuli of all clusters (high- z and low- z always separately). However, stacking the X-ray sources found in different pointings of the XMM-LSS field is only possible if we eliminate the systematic differences in the exposure time, background, and off-axis distance. To this end, we multiply the sources found within a certain annulus in a cluster by a weight w_{ij} , where i is the number of the annulus and j refers to the cluster, to elim-

inate the above differences. In the case of the low- z sample, the weight of an annulus i of a cluster j is

$$w_{ij} = N_{f\ ij} / N_{\text{exp}\ ij} ,$$

where $N_{f\ ij}$ is the number of sources in the annulus i of cluster j , calculated directly from the $\log N - \log S$ before applying the corrective factors of steps 2-4 of §2.2, and thus it does not include any information about the exposure time, background, and off-axis distance, whereas $N_{\text{exp}\ ij}$ is the number of expected sources that does include these corrections (see §2.2). We stress that the weighting is essential because we want to estimate the overdensity of the merged annuli by the formula:

$$\Delta_i = \left(\sum_{j=1}^K N_{ij} / \sum_{j=1}^K N_{\text{exp}\ ij} \right) - 1 .$$

where N_{ij} is the number of detected x-ray sources and $N_{\text{exp}\ ij}$ as before. The outcome of the formula is not the average overdensity of the clusters, since we are not adding the individual cluster overdensities, but rather the total overdensity of the stacked regions, as we are summing the number of sources of all clusters. Consequently, we calculate the total X-ray source merged overdensity in the annulus i by the formula:

$$\Delta_i = \left(\sum_{j=1}^K N_{ij} w_{ij} / \sum_{j=1}^K N_{\text{exp}\ ij} w_{ij} \right) - 1 ,$$

where K is the number of clusters. This procedure corrects the number of observed sources to the number that we would have found in any certain annulus within the XMM-LSS field if not for the differences in exposure time, background and off-axis distance.

For the stacking analysis of the high- z sample clusters we need to add an extra correction, which occurs because the lower flux limit is now fixed to the survey's lower limit of 3×10^{-15} erg $\text{s}^{-1} \text{cm}^{-2}$ (see §2.1) independently of the redshift. This flux corresponds to a different limiting $L_{x,\text{lim}}$ in each cluster. Thus, as we go to higher redshift, the flux limit remains the same but the effective area under investigation for a given r_{500} radius is getting smaller resulting in a progressively smaller number of expected or actually detected sources. For example, considering the same cluster at two different redshifts, the projected r_{500} radius in arcmin is larger at the lower redshift. With a fixed lower flux limit, the number of expected and detected sources in the larger area at the lower redshift is larger, rendering the low-redshift cluster "heavier" in the stacking procedure, since it contributes more in the sum of the sources. To minimize this effect, we choose a random cluster, we set it as reference, and we normalize the area of every sample cluster to the respective one of the reference cluster. The normalization should not eliminate the intrinsic r_{500} area differences, i.e. should correct only for the redshift difference of the clusters. Therefore, the weight formula is now transformed to

$$w_{ij} = \frac{N_{f\ ij}}{N_{\text{exp}\ ij}} \times \frac{A_{\text{ref}}}{A_j} \times \frac{B_j}{B_{\text{ref}}} ,$$

where A_{ref} and A_j are the projected reference and cluster area in deg^2 , respectively, whereas B_{ref} and B_j are the intrinsic reference and cluster area in Mpc^2 , respectively. The second term normalizes all cluster areas to the reference area, while the third enforces the intrinsic differences of r_{500} between different clusters. In that way we add all sources found above the constant

lower flux limit, within the respective r_{500} annuli of any cluster, free of the progressive area-diminishing effects. Consequently, as already mentioned, the stacking for the high- z clusters is conducted between a range of different limiting X-ray AGN luminosities ($\sim 1.7 \times 10^{42} - 1.4 \times 10^{43}$ erg/s), although this range is not that wide. This caveat is also present in most other studies that use a fixed lower flux limit and not a luminosity one (Haines et al. 2012; Ehlert et al. 2014; Fassbender et al. 2012; Martini et al. 2013). The comparison between these studies is even more difficult due to the different redshift regimes under investigation, leading to a progressive loss of the less powerful AGN population with distance. However, although a direct comparison between the low and high-redshift clusters is not possible in the current study or between other studies, sample in two), pointing out differences and similarities can still be useful.

Finally, we calculate the Poissonian error on the weighted number n of events, given by the formula:

$$\sigma \left(\sum n \right) = \sigma \left(\sum w \right) = \left(\sum w_i^2 \right)^{1/2} .$$

The number of optical galaxies, in each annulus, does not have to be corrected before stacking, since optical data in the CFHTLS do not suffer from any obvious incompleteness or any other selection effect up to $i_{\text{mag}} \simeq 24$. This limit is adequate for the present study, since we only have to exclude one cluster from the optical analysis, XLSSC 078.

2.6. Spatial overdensity analysis using redshifts and visual inspection of counterparts

To interpret our results and attempt to understand the physical mechanisms behind the observed X-ray overdensities, we would ideally like to be able to place the candidate X-ray AGN in the cluster or its outskirts. Spectroscopy, however, is only available for $\sim 24\%$ of our X-ray point-like sources (Table 1), and thus we investigate the rest of the objects based on photometric redshifts and visual inspection. Calculation of the photometric redshifts is described shortly in this section and in more detail in Melnyk et al. (2013).

For each X-ray source, we take only one best rank optical CFHTLS counterpart into account, based on its distance from the X-ray source and its relative brightness (rank=0 for a single very reliable counterpart or 1 for a less reliable but preferred counterpart, see Chiappetti et al. 2013 for details). All counterparts with less than four available photometry bands were also discarded. We therefore only considered 4555 point-like X-ray sources ($\sim 72\%$ completeness), 4450 of which have spectroscopic or photometric redshifts with $z > 0$ (non-stars). The list of redshifts for all XMM-LSS sources can be found in Table 2 of Melnyk et al. (2013). For the photo- z determination, the LePhare⁴ public code (Arnouts et al. 1999, Ilbert et al. 2006) was used. The accuracy⁵ of the photometric redshift calculation is $\sigma_{\Delta z / (1+z_{\text{sp}})} = 0.076$, with 22.6% of them outliers for the case of counterparts having at least four photometric bands. The redshift probability distribution (PDZ) of $\sim 41\%$ of the sources is PDZ=100, meaning that the solution is unique and highly probable. The bulk of our sources, with unavailable spectroscopic redshifts, are from the above subsample, or they have photometric redshifts calculated with at least seven bands. The latter have PDZ<100, meaning larger uncertainties, although the spectro- z to photo- z relation is similar to that of the PDZ=100 sources (see

⁴ <http://www.cfht.hawaii.edu/~arnouts/LEPHARE/lephare.html>

⁵ $\sigma_{\Delta z / (1+z_{\text{sp}})}$ according to Hoaglin et al. (1983)

Melnyk et al. 2013). The LePhare code also indicates secondary solutions, but in this case the sources were rejected. Double-peak solutions are produced when only a few photometry bands are available, and that happens mostly in the ABC supplementary fields.

Any X-ray counterpart to be considered as a cluster member should have its spectroscopic redshift within $\pm 2000\text{km/s}$ of the cluster redshift z_{cl} , or photometric redshift z_{ph} within $\sigma(1 + z_{cl})$, where $\sigma=0.065$ to 0.076 depending on the available photometry bands that were used for the calculation and the redshift probability distribution (Melnyk et al. 2013).

For the CFHT optical galaxies we used the photometric redshifts of the CFHTLS-T0007 W1 field (Ilbert et al. 2006 and Coupon et al. 2009) computed for three to five optical bands. The accuracy is 0.031 at $i < 21.5$ and reaches $\sigma_{\Delta z/(1+z_{sp})} \sim 0.066$ at $22.5 < i < 23.5$. The fraction of outliers increases from $\sim 2\%$ at $i < 21.5$ to $\sim 10 - 16\%$ at $22.5 < i < 23.5$. More details about the photometric redshift calculation can be found in the explanatory document⁶.

With all the above data available, we can produce again the stacked overdensities, but this time in three-dimensional space. For calculating the expected field objects for both X-ray sources and optical galaxies, we again use the same criteria and the same catalogs in a $\sim 2 \text{ deg}^2$ field. This is very important, especially for the X-ray counterpart’s photometric catalog that is not complete, so that the overdensity measurements would not be affected.

Finally, using the SDSS⁷ and CFHT databases, we visually inspected all the counterparts of the X-ray point-like sources within $4r_{500}$ (or $5r_{500}$ for the high- z sample) of every cluster. Our aim was to combine the available redshifts and images, to provide a more reliable list of cluster members and background/foreground objects, by investigating the morphology of cluster members, and assessing the probability of sources with no redshift of also being cluster members. Visual inspection is the only tool we have for the fraction of our sources that do not have photometric redshifts, either because there was no counterpart found or because the available photometric bands were less than four. However, by comparing them to the rest of the population we get hints about their redshift and their candidacy as cluster members. In fact, most of these appear to be blue point-like sources that are very similar to the spectroscopically confirmed background sources. The rest are either very faint or with no counterpart, and it seems that they are even less likely to be correlated with the clusters (see also relative discussion in Ehlert et al. 2014). All our results can be found in Table 1 and 2.

3. Results

3.1. X-ray point source overdensity

Using the methodology of §2.2, we calculate the X-ray point source overdensities of all our sample clusters in annuli up to $5r_{500}$ ($6r_{500}$ for the high- z sample) where we expect to have reached the field density. However, the number of sources found in each cluster is small, especially in the first annulus, which not only is the smallest one, but is also the one that includes the extracted core (25% of its area). To address this issue and derive more robust results, we stacked all clusters of each subsample (high- z and low- z separately), calculating the total overdensity for each annulus as described in §2.5. Nevertheless, in what follows we also present the results of all clusters individually, while we list all data in Tables 1 and 2.

In Fig. 4 we present the stacking results of the low- z clusters (left panel) and of the high- z clusters (right panel). We can see that for the low- z (high- z) clusters, in the first (and second) annulus, the X-ray overdensity is high and it drops steeply in the second (third) annulus. However, this behavior is reversed in the next annuli, where the overdensity rises again until it drops and converges to the background zero level in the fifth (sixth) annulus. The X-ray point source excess in the first annulus of both the low and the high-redshift samples is to be expected, since as already mentioned, it is reported in numerous previous studies (e.g., Cappi et al. 2001, Molnar et al. 2002, Johnson et al. 2003, D’Elia et al. 2004, Gilmour et al. 2009, Melnyk et al. 2013). The extension of the excess in the second annulus for the high- z sample could be due to intrinsic differences of the two sets of clusters or evolutionary effects in the dynamics of the clusters.

In addition, the overdensity “bump” at larger radii is statistically significant and is present in both our cluster samples that are completely independent. The fact that the rise is not appearing at the same scale for both samples of clusters could be again due to the above-mentioned differences in the two.

This excess has been reported in previous studies (Ruderman & Ebeling 2005; Fassbender et al. 2012) and has been attributed to an infalling population of galaxies in the outskirts of the clusters that interacts and merges, producing an overdensity of X-ray AGN in the area. In addition, Haines et al. (2012) compared infalling with virialized populations and concluded the same. Although the analysis of Ehlert et al. (2014) stops at $2.5r_{500}$, the start off the “bump” is already apparent after $2r_{500}$, but the authors do not comment on that assuming that the cluster X-ray source density converges to the expected field value at distances of $\sim 2r_{500}$. In contrast, Gilmour et al. (2009) argue that any X-ray point source overdensity found at large radii is due to additional clusters in or near the field of view, which may also contain AGN and probably also contributes to the enhancement of background AGN. This surplus is confirmed for our low-redshift clusters at a smaller radial distance compared to previous works, i.e. for the current study approximately between 1 and 2 Mpc but between 2 and 3 Mpc for rich clusters. Nevertheless, our high- z clusters are more comparable to rich clusters since their excess is found after 1.5 Mpc. This comparison to other studies should be considered with caution owing to the different methods used for the stacking, i.e. stacking the same radii in arcmin, Mpc or r_{500} . Nevertheless, the results appear to be expected considering that, on physical scales, the outskirts of poor and moderate clusters should be closer to the center of each cluster. This difference is already present even between our two samples that consist of clusters with different “richness” (see Tables 1 & 2).

3.2. X-ray point source versus optical galaxy overdensity

3.2.1. Stacking analysis

As a next step it is essential to compare the already found X-ray point source overdensities to the optical galaxy overdensities. Following the methodology presented in §2.4, we calculate the stacked overdensity of optical galaxies for the clusters that fall within the CFHTLS area (twelve of the low- z and eight of the high- z sample; $\sim 60\%$ of each). We do not expect that the optical galaxy overdensity profile would vary if we had added the missing clusters to its calculation. Nevertheless, to verify that the comparison between X-ray and optical overdensity is not affected, we also limited our X-ray analysis to only the clusters covered by the CFHTLS and reached the same conclusions.

⁶ ftp://ftpix.iap.fr/pub/CFHTLS-zphot-T0007/cfhtls_wide_T007_v1.2_Overview.pdf

⁷ <http://www.sdss3.org/>

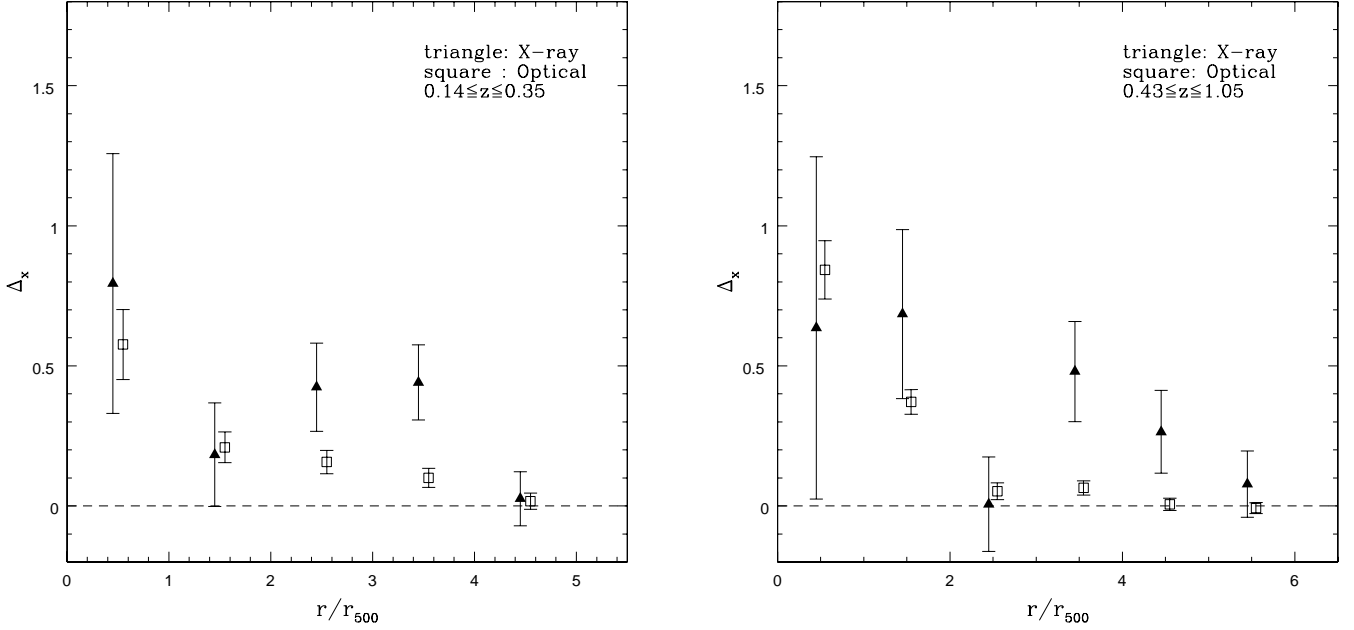


Fig. 4. Stacked optical galaxy overdensity (open squares) vs X-ray point source overdensity (triangles) as a function of projected cluster-centric distance. Uncertainties are 1σ Poissonian errors of the weighted number of objects. *Left Panel:* Low- z cluster sample. *Right Panel:* High- z cluster sample.

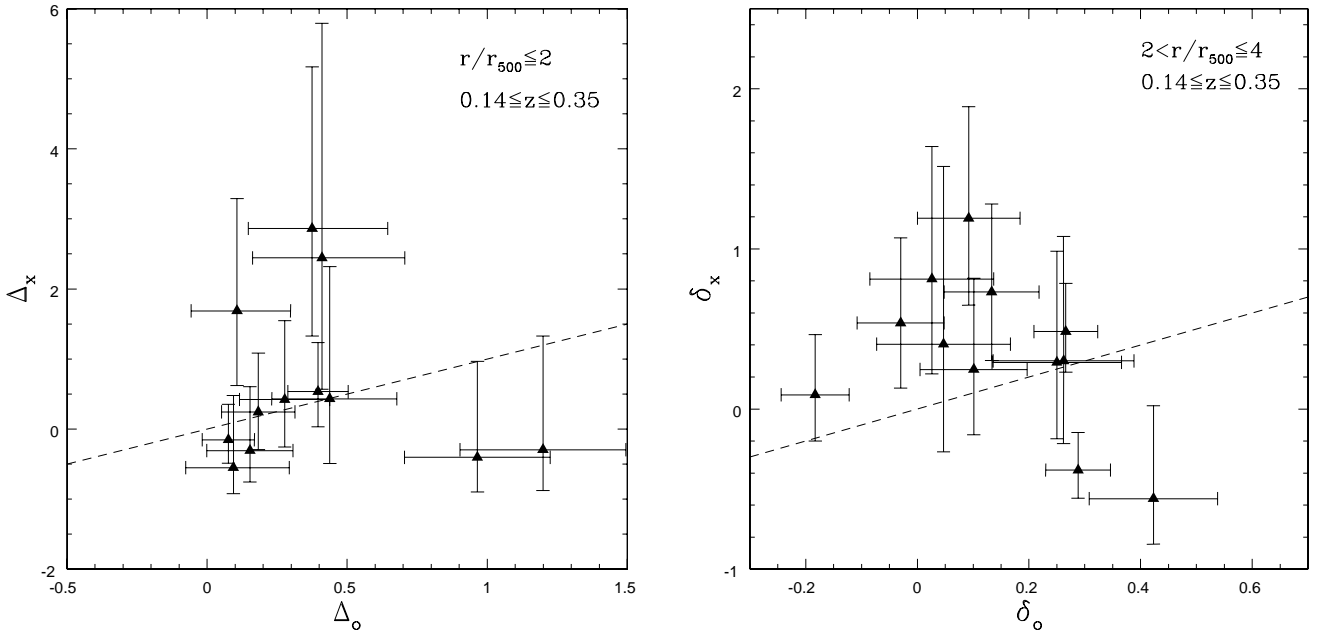


Fig. 5. Optical galaxy overdensity vs X-ray point source overdensity for each low- z cluster individually. The dashed line corresponds to $\Delta_x = \Delta_o$. Uncertainties are Poisson 1σ errors for small numbers (Gehrels 1986).

Therefore, in Fig. 4 we overplot the optical profile to the X-ray overdensity data. For the low- z sample (left panel of Fig. 4) the X-ray overdensity profile is consistent with the corresponding optical one in the first two annuli. Especially in the first one even a small X-ray excess can be seen, but it is within the 1σ errors and thus not statistically significant. Similar results are also found for the high- z sample (right panel of Fig. 4), where the X-ray overdensity exhibits a more prominent excess in the second

bin and agrees with the optical galaxy overdensity in the third. Overall, we conclude that within the first bins the X-ray overdensity is as expected by the respective optical galaxy results. This contradicts to the X-ray AGN suppression that many previous studies of rich clusters have reported (e.g., Koulouridis & Plionis 2010; Ehlert et al. 2013; Haines et al. 2012). Nevertheless, we should note once more that the current samples consist of intermediate and low-luminosity clusters in which the triggering and

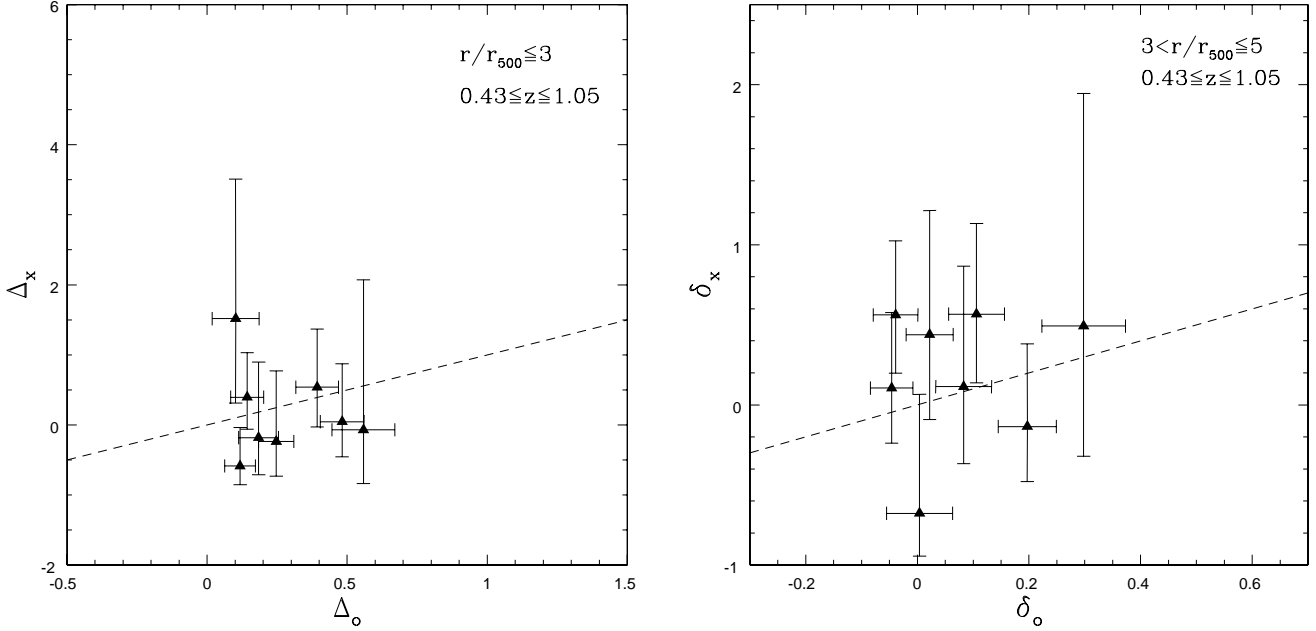


Fig. 6. Optical galaxy overdensity vs X-ray point source overdensity for each high- z cluster individually. The dashed line corresponds to $\Delta_x = \Delta_o$. Uncertainties are Poisson 1σ errors for small numbers (Gehrels 1986).

feeding of the AGN may be more favorable than in richer clusters. In addition, the BCGs, which in many cases host an AGN, are excluded (since the central region is excluded). The extra X-ray AGN would increase the X-ray overdensity dramatically, but we argue that the BCG’s path of evolution is very different from the other cluster galaxies and should be excluded for the purposes of the current analysis.

Following the steep drop a rise in the X-ray overdensity occurs again in the next two bins, but does not appear in the optical data. Then, they both converge to the background level in the respective last annulus of our analysis. Thus, this distant X-ray overdensity “bump”, which was discovered in the previous section of the current study, presents statistically significant differences when also compared to the optical galaxy overdensity for both our samples. Consequently, we argue that the abundance of X-ray sources in large clustercentric radii around rich clusters is replicated in poor and intermediate clusters, although in somewhat smaller physical distances.

3.2.2. Individual cluster analysis

After completing the stacked analysis, we would also like to investigate the behavior of individual clusters, to clarify if the discrepancies between optical galaxy and X-ray point source overdensities emanate from the behavior of all the clusters in the samples or just a subsample. Only clusters located in the CFHTLS region are used in the current analysis, as explained in the methodology.

In Fig. 5 we plot the X-ray vs the optical overdensity for the low- z sample up to the second annulus (left panel) and from the third up to the fourth (right panel) for each cluster separately. We selected only those bins in which a positive X-ray overdensity is found, excluding the last annulus where it drops to zero. Judging by the r_{500} values (Table 1) we can estimate that the $2r_{500}$ radius corresponds to ~ 1 Mpc radial distance. Therefore, for poor clusters, Fig. 5 is analogous to Fig. 1 of Koulouridis &

Plionis (2010) for rich Abell clusters. We see that for the first two bins more than half of our sample clusters are located close to the dashed line that denotes equality between optical and X-ray overdensities, while the rest are on the one or the other side, canceling out any discrepancy. However, in the next two bins all but two clusters move above the line (even marginally) and that is the reason for the discovered X-ray overdensity “bump”.

We also plot the individual cluster overdensities for the high- z sample in Fig. 6. To trace the same trends and compare with Fig. 5, we add the first three annuli in the left-hand panel and the next two on the right. Qualitatively, the results are similar to what we found in Fig. 5. The X-ray “bump” discovered again at larger distances from the cluster center seems to be produced by a rise in the X-ray point source density in almost all the clusters.

These results do not agree with the analysis of Gilmour et al. (2009), where the excess overdensity was attributed solely to additional X-ray AGN and/or lensing due to foreground or background clusters in or near a small fraction of their sample clusters, although the extra lensing seems to be true for some of our low-redshift clusters that happen to have a background cluster projected within their area. In Fig. 7 we present an example of such a case where XLSSC 010 is the foreground cluster at redshift $z=0.33$ and XLSSC 003 the background one at redshift $z=0.84$. In the fourth bin of XLSSC 010 about seven sources are expected but 14 found, out of which seven or eight are found in the conjunction of the outer bins of both clusters.

We stress that the results based on the individual and the stacked cluster analysis are not directly comparable, because only clusters that are located in the CFHTLS region are included in the individual analysis, while we use the full sample for the X-ray stacked analysis. In addition, no weighting is performed in the individual analysis, thus adding the individual cluster overdensities will not result in the stacked one. On the other hand, most of our clusters exhibit high X-ray source overdensities without any other cluster visible on their background. We will

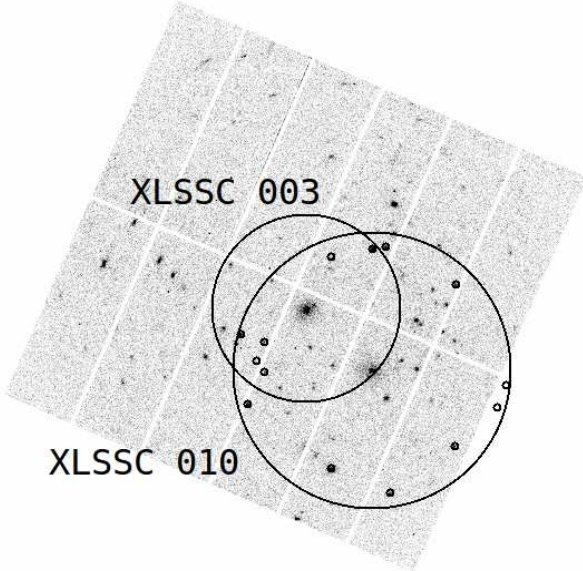


Fig. 7. XMM-Newton image of galaxy clusters XLSSC 010 ($z=0.33$) and XLSSC 003 ($z=0.84$). The large circles mark the $4r_{500}$ radius of XLSSC 010 and the $5r_{500}$ radius of XLSSC 003, while the small ones point toward the detected X-ray point-like sources within the fourth annulus of the low-redshift cluster. More than half of the sources seem to be concentrated in the conjunction of the outer annuli of the two clusters.

probably need to conduct the same study to the full XXL survey in order to clarify this issue.

3.3. Spatial overdensity analysis

Having discovered that the X-ray sources exhibit excessive values of overdensity, not only in the first annuli where they are consistent with the optical galaxy excess, but also at larger distances where they are significantly higher, it is very important to determine whether this excess is real, i.e., if it can be attributed to cluster members. To this end, we used the available spectroscopic and photometric redshifts and the methodology of §2.6. We should note that we are forced to use larger bin separation in order to have more meaningful results because the number of clusters that have available photometric redshifts is still small. For the low-redshift clusters we merge the first two bins in one and the next three bins as well, resulting in a total of two bins, while for the high-redshift clusters we use three bins in total.

In Fig. 8 we present the results of the spatial analysis for the low- z and high- z cluster samples (left and right panels, respectively). We also plot the results when including the ABC region, where the photometric redshifts of the X-ray sources were calculated with fewer bands. We can see that the uncertainties are still very large for the X-ray sources, despite the merging of the annuli. For the low- z sample, in the first bin, which corresponds to the first two annuli in the projected analysis, the X-ray and the optical overdensities seem to agree, as they also did in the projected overdensity analysis. However, the excess in the second bin, which corresponds to the third and fourth annuli in the projected analysis, has disappeared. Overall, the number of X-ray-selected AGN found within the three cluster bins is exactly the same as found in the field. This sharp contrast with our previous projected overdensity results is probably due to lensing

of background sources that can affect the projected overdensity analysis but not the spatial one.

Our high- z sample exhibits a different behavior. The total overdensity of X-ray-selected AGN in the area of clusters is higher than what is expected, but up to $4r_{500}$ is practically zero (although with large uncertainty) and rises in the last merged bin. In addition, the difference with the optical galaxy overdensity is significant in this last bin, since the AGN found are more than double what is expected. Adding the ABC fields only brings the X-ray overdensity closer to the optical in the first merged bin but does not change the results of the other two.

Overall, the trend of X-ray AGN deficiency in rich galaxy clusters cannot be confirmed for the low- z clusters, while for the intermediate ones of the high- z sample, a suppression is possible in the bins closer to the center, but the results are dubious because of small number statistics. Nevertheless, the number of X-ray counterparts that are confirmed in the outer annuli of the high- z sample seems to corroborate previous results that report an excess of X-ray AGN in the outskirts of clusters. This is only true for the richer clusters, probably because these are more massive structures, still accreting galaxies that are gathering in the outer parts of the clusters and are effectively interacting before entering the potential of the cluster and the hot ICM.

Considering that redshifts are not available for a large number of X-ray sources, we proceed with the visual inspection of all the counterparts of the cluster member candidates of the projected overdensity analysis up to the 4th bin (5th bin) for the low- z (high- z) sample. Our aim is to investigate the morphology of the optical counterparts of the confirmed X-ray AGN cluster members and compare them to the ones that lack any redshift information. We should mention, however, that no counterpart is detected in many cases or the determination of the correct counterpart is dubious.

In Table 1 (columns (12) – (20)) we present our results for the low- z sample. The first four columns ((12) – (15)), which correspond to the four r_{500} annuli respectively, contain the number of sources that, based on the redshift of their optical counterparts, are background or foreground (projected) objects. The following four columns ((16) – (19) that correspond to the same four r_{500} annuli) instead contain the sources that are true cluster members (not included in the projected sources). In column (20) we report the sources that lack any redshift information. Therefore, the sum of the nine columns ((12) – (20)) is the total number of X-ray sources N_x in all the cluster’s annuli, reported in column (11). The numbers in parenthesis are the sources with available spectroscopic redshift and are a subsample of the preceding number of sources, e.g., 8(3) in column (14) of Table 1 shows that from the total eight sources with redshift information in the third bin, three have spectroscopic redshifts and five photometric. Clusters located in the ABC supplementary fields, where the majority of the photometric redshifts of the counterparts are of poor quality, are marked with an x sign in column (21), and the respective photometric redshifts are placed within brackets. Table 2 includes the high- z sample, with the only difference that the number of columns that correspond to the cluster’s annuli are in this case five (see §3.1).

From the total of 274 sources in the low- z clusters, $\sim 30\%$ have spectroscopic redshifts, which rises to 35% if we exclude the ABC fields. On the other hand, objects with no redshift information are the 22% of the total, but that percentage drops to 10% when excluding the ABC fields. The majority of the non-redshift X-ray sources are blue point-like objects. These counterparts are abundant in our sample, and when redshift is available, they can securely be classified as background QSOs. We have no reason

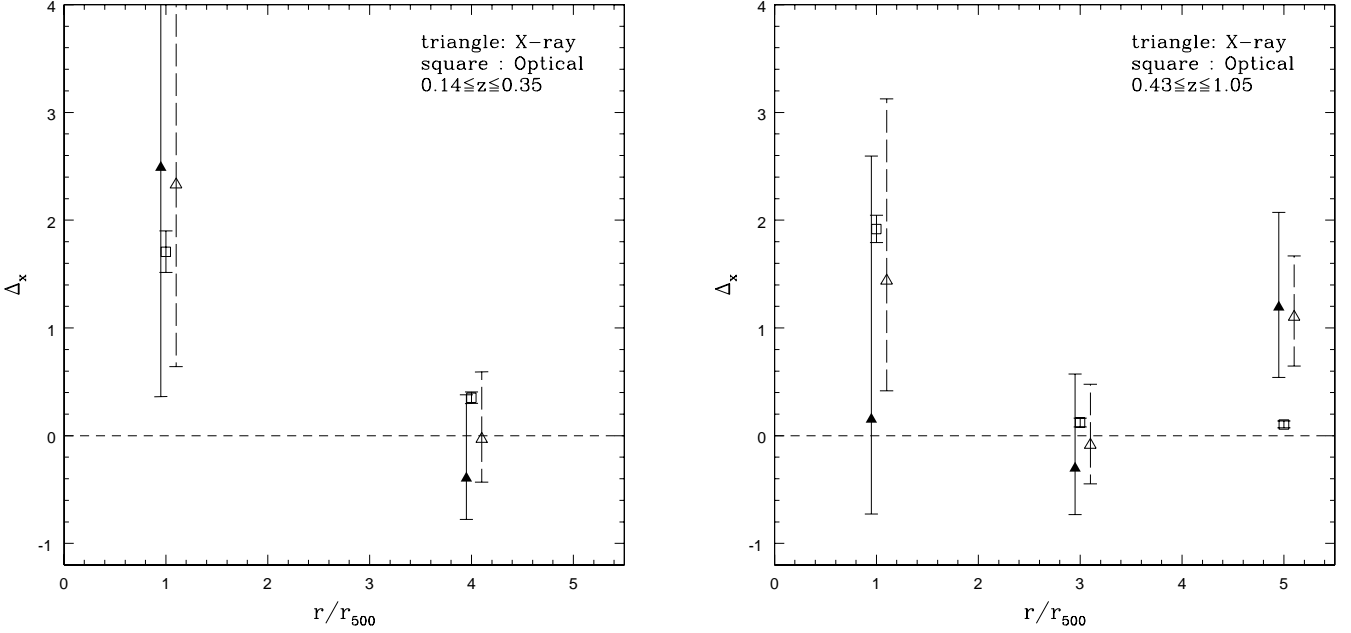


Fig. 8. Spatial stacked optical galaxy (open squares) and X-ray point source overdensities as a function of projected radial distance from the center of the cluster, including only clusters in the CFHTLS region (solid triangles) and including clusters in the CFHT ABC supplementary pointings (dashed triangles). *Left panel:* The low- z cluster sample. *Right panel:* The high- z cluster sample. Uncertainties are Poisson 1σ errors for small numbers (Gehrels 1986).

to believe that these sources belong to any of our clusters. Apart from those, a large fraction of non-redshift objects do not have any counterpart. Finally, only a small number of objects look like faint normal galaxies that may or may not be cluster members, while the reported redshift of a few others seems improbable. In Tables 1 & 2 we included or excluded such objects accordingly. Judging from the results of objects with available redshift, we argue that the probability of sources with no available redshift to be cluster members is very low, especially for the clusters that fall in the CFHTLS region. Thus, we argue that not considering them in the spatial analysis of our samples does not alter our results.

We conducted the same analysis for our high-redshift clusters, and found that from the total of 233 sources 17% have spectroscopy, which rises to 30% if we exclude the ABC fields. On the other hand, objects with no redshift information are the $\sim 20\%$ of the total, similar to the low- z sample.

SDSS images of the optical counterparts of the 15 X-ray AGN located within the first r_{500} annulus of the 19 low-redshift ($0.14 \leq z \leq 0.35$) clusters can be found in Fig. 9. Only XLSSC 025(2) is a confirmed cluster member, while most of the rest counterparts are blue point-like background objects. Also, some examples of CFHT i-band images of X-ray source counterparts, with photometric or spectroscopic redshifts that indicate they are true cluster members, can be seen in Fig. 10. Their extended morphology is a further evidence that they are not projected background QSOs.

4. Conclusions

We conducted a statistical study of 33 clusters of poor and moderate richness, within the XMM-LSS field that covers $\sim 20\%$ of the XXL survey, by comparing the density of X-ray sources within multiples of the r_{500} radius with the expected field den-

sity, calculated from the $\log N - \log S$ for the same area. We compared this projected overdensity with the respective optical galaxy overdensity in an attempt to estimate the suppression or the enhancement of X-ray-selected AGN. In addition, we calculated the spatial overdensities, using the available spectroscopic and photometric redshifts in an attempt to identify and quantify the true cluster members and explain the results of our previous projected analysis.

The conclusions that can be drawn from the above analysis are the following:

- The projected analysis of X-ray versus optical overdensity within the two central r_{500} annuli, corresponding to ~ 1 Mpc radius, results in a strong positive signal showing that the environment of the low and moderate X-ray-luminosity clusters of our samples does not suppress the X-ray AGN activity. This result is in sharp contrast to the outcome of many studies of rich clusters (e.g., Koulouridis & Plionis 2010; Ehlert et al. 2013; Haines et al. 2012), which implies that lower richness cluster environments do not suppress X-ray AGN activity. Interestingly, in even lower density environments (galaxy groups), an enhancement of X-ray AGN may be present (Melnik et al. 2013).

- After calculating the projected overdensities at large radial distances from the center of the cluster ($3^{rd} - 5^{th}$ bins, corresponding to $\sim 1.5-3$ Mpc, depending on the redshift), a significant rise in the X-ray source overdensity is observed. This excess has also been reported in previous studies (Haines et al. 2012, Fassbender et al. 2012) and has been attributed to an infalling population of galaxies from the outskirts of the clusters that interact and merge, producing the observed overdensity of X-ray AGN. This surplus is confirmed for both our low- and high-redshift clusters.

- Using spectroscopic and photometric redshifts, we discovered that the X-ray “bump” at a large radial distance vanishes completely from the poor low- z sample, and we argue there-

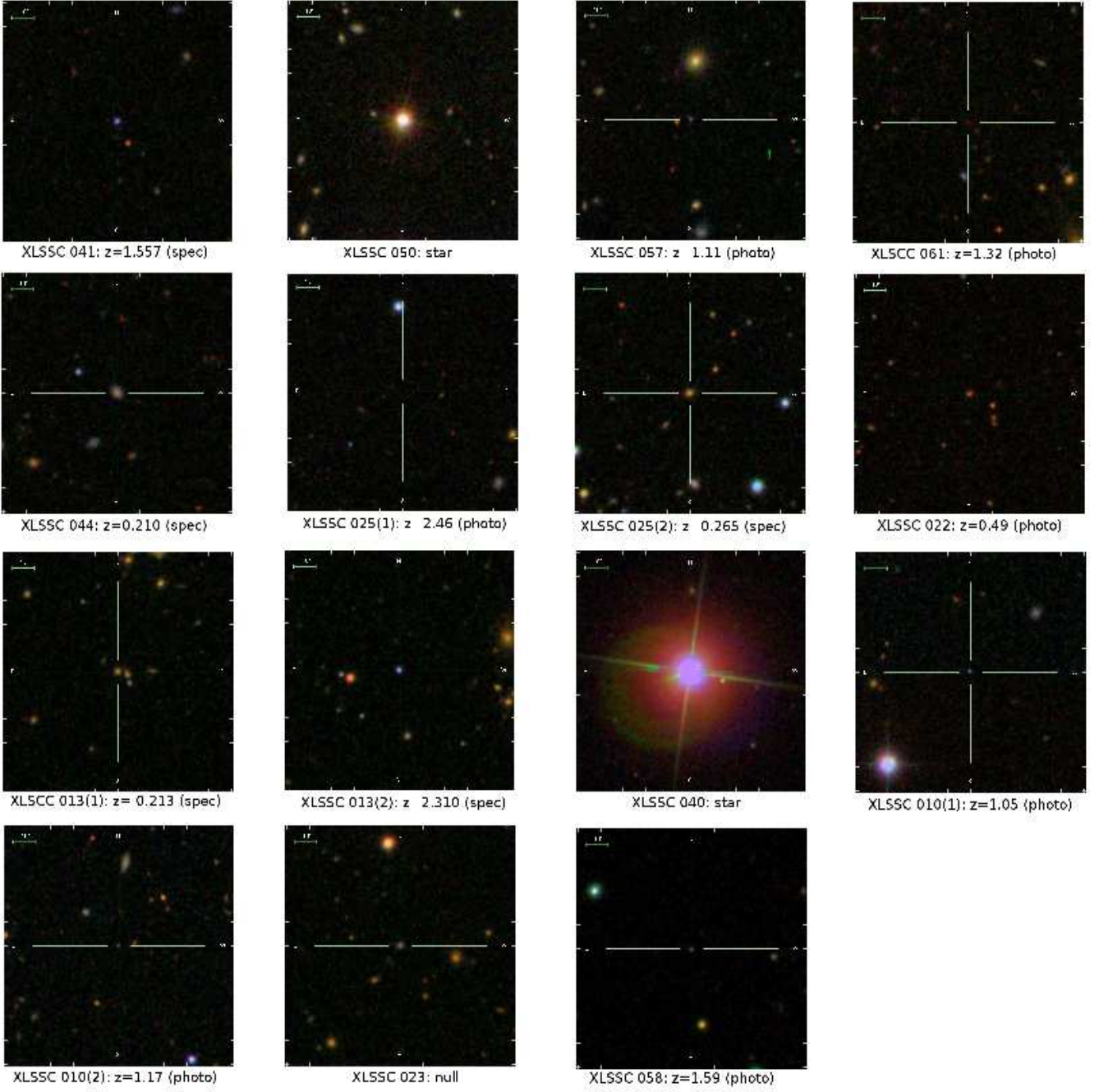


Fig. 9. SDSS images of the 15 sources located within r_{500} from the center of the 19 low-redshift ($0.14 \leq z \leq 0.35$) clusters. Only XLSSC 025(2) is a confirmed cluster member. In the parenthesis we indicate if the redshift is spectroscopic or photometric. The scale can be seen in the upper left corner of each image.

fore that this density excess may be produced by flux boosting of background sources due to gravitational lensing, sometimes even enhanced by additional background galaxy clusters along the same line of sight. On the other hand, a high X-ray source overdensity persists in the last annulus of the moderate X-ray luminosity high- z sample, implying that for intermediate “richness” clusters, additional triggering of X-ray AGN in the outskirts is still possible.

In a nutshell, the projected overdensity analysis produces statistically significant results, but at the same time these results are contaminated by projection effects of background-lensed QSOs. On the other hand, although the spatial analysis performed is

free of these effects, it is not able to reach definite results owing to the small numbers involved, making it necessary to study larger samples of galaxy clusters. Especially the area included in the annuli closer to the cluster center is so small that does not allow us to reach any definitive conclusions about the suppression of X-ray AGN. The stacking of clusters proves very useful, but splitting the total sample into two redshift subsamples again reduces the numbers greatly. However, the division is crucial since not only do we select a population of more X-ray luminous clusters in higher redshifts, but we can also detect only higher luminosity X-ray AGN.

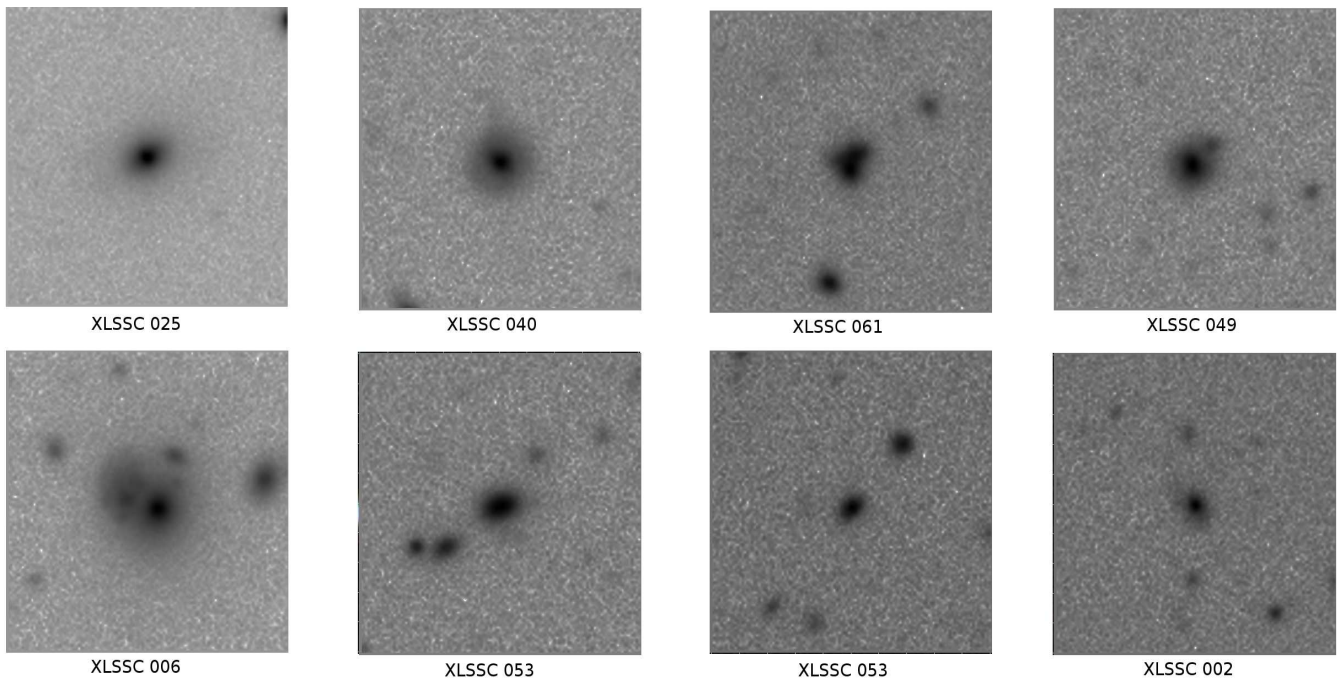


Fig. 10. Examples of CFHTLS i-band images of X-ray source counterparts, with photometric or spectroscopic redshifts indicative of them being true cluster members. The dimensions of each image is $30'' \times 30''$

We should stress that the large contiguous area of the XMM-LSS has allowed us to study the overdensity of X-ray AGN within large radial distances from the cluster center for the first time. This proved to be essential for exploring the relation between the dense environment of clusters and the X-ray AGN activity in detail. To fully understand this relation, we need to trace its evolution as a galaxy approaches the cluster's gravitational potential, enters the hot ICM, and crosses the cluster. At the same time, we need to disentangle irrelevant effects such as the gravitational lensing of background sources, probably enhanced by the presence of additional clusters along the line of sight. A photometric variability study of these sources may also shed some light on whether the lensing amplification could be due to micro-lensing and/or convergence by matter in the clusters.

We believe that the analysis of the full XXL field, which is almost five times larger than the XMM-LSS (reaching 50 deg^2), together with a detailed spectroscopic follow-up of the optical counterparts of all X-ray point sources, detected in the XXL clusters, may provide reliable and robust results as to the origin (true enhancement, lensing, presence of background clusters, etc) of the excess X-ray sources detected in the outer $\sim 3 - 5r_{500}$ annuli of either low and high-redshift clusters.

Acknowledgements. We would like to thank the anonymous referee who provided insightful comments and suggestions. EK acknowledges fellowship funding provided by the Greek General Secretariat of Research and Technology in the framework of the programme Support of Postdoctoral Researchers, PE-1145. This work is based on observations obtained with XMM-Newton, an ESA science mission with instruments and contributions directly funded by ESA Member States and the USA (NASA). Funding for SDSS-III has been provided by the Alfred P. Sloan Foundation, the Participating Institutions, the National Science Foundation, and the U.S. Department of Energy Office of Science. The SDSS-III web site is <http://www.sdss3.org/>. This work is based on observations obtained with MegaPrime/MegaCam, a joint project of CFHT and CEA/IRFU, at the Canada-France-Hawaii Telescope (CFHT) which is operated by the National Research Council (NRC) of Canada, the Institut National des Sciences de l'Univers of the Centre National de la Recherche Scientifique (CNRS) of France, and the University of Hawaii. This work is based in part on

data products produced at Terapix available at the Canadian Astronomy Data Centre as part of the Canada-France-Hawaii Telescope Legacy Survey, a collaborative project of NRC and CNRS.

References

- Aarseth, S. J., & Fall, S. M. 1980, *ApJ*, 236, 43
 Abell, G. O. 1958, *ApJS*, 3, 211
 Adami, C., Mazure, A., Pierre, M., et al. 2011, *A&A*, 526, A18
 Alshino, A., Ponman, T., Pacaud, F., & Pierre, M. 2010, *MNRAS*, 407, 2543
 Arnold, T. J., Martini, P., Mulchaey, J. S., Berti, A., & Jeltema, T. E. 2009, *ApJ*, 707, 1691
 Balogh, M. L., Navarro, J. F., & Morris, S. L. 2000, *ApJ*, 540, 113
 Balogh, M., Bower, R. G., Smail, I., et al. 2002, *MNRAS*, 337, 256
 Barnes, J. E., & Hernquist, L. E. 1991, *ApJ*, 370, L65
 Bekki, K., Couch, W. J., & Shioya, Y. 2002, *ApJ*, 577, 651
 Best, P. N. 2004, *MNRAS*, 351, 70
 Best, P. N., Kauffmann, G., Heckman, T. M., et al. 2005, *MNRAS*, 362, 25
 Best, P. N., von der Linden, A., Kauffmann, G., Heckman, T. M., & Kaiser, C. R. 2007, *MNRAS*, 379, 894
 Branchesi, M., Gioia, I. M., Fanti, C., Fanti, R., & Cappelluti, N. 2007, *A&A*, 462, 449 bibitem[Brandt & Alexander(2010)]2010PNAS..107.7184B
 Brandt, W. N., & Alexander, D. M. 2010, *Proceedings of the National Academy of Science*, 107, 7184
 Cappelluti, N., Hasinger, G., Brusa, M., et al. 2007, *ApJS*, 172, 341
 Cappi, M., et al. 2001, *ApJ*, 548, 624
 Chiappetti, L., Tajer, M., Trinchieri, G., et al. 2005, *A&A*, 439, 413
 Chiappetti, L., Clerc, N., Pacaud, F., et al. 2013, *MNRAS*, 429, 1652
 Cisternas, M., Jahnke, K., Inskip, K. J., et al. 2011, *ApJ*, 726, 57
 Cooper, M. C., Newman, J. A., Coil, A. L., et al. 2007, *MNRAS*, 376, 1445
 Cowie, L. L., & Songaila, A. 1977, *Nature*, 266, 501
 Cypriano, E. S., Sodré, L. J., Campusauro, L. E., Dale, D. A., & Hardy, E. 2006, *AJ*, 131, 2417
 D'Elia, V., Fiore, F., Elvis, M., Cappi, M., Mathur, S., Mazzotta, P., Falco, E., & Cocchia, F. 2004, *A&A*, 422, 11
 Davis, D. S., Miller, N. A., & Mushotzky, R. F. 2003, *ApJ*, 597, 202
 Dressler, A., Thompson, I. B., & Shectman, S. A. 1985, *ApJ*, 288, 481
 Eastman, J., Martini, P., Sivakoff, G., Kelson, D. D., Mulchaey, J. S., & Tran, K.-V. 2007, *ApJ*, 664, L9
 Ebrero, J., Mateos, S., Stewart, G. C., Carrera, F. J., & Watson, M. G. 2009, *A&A*, 500, 749
 Edge, A. C., & Stewart, G. C. 1991, *MNRAS*, 252, 414
 Edge, A. C., & Stewart, G. C. 1991, *MNRAS*, 252, 428

- Ehlert, S., Allen, S. W., Brandt, W. N., et al. 2013, *MNRAS*, 428, 3509
- Ehlert, S., der Linden, A. v., Allen, S. W., et al. 2013, *MNRAS*, 2681
- Ellison, S. L., Patton, D. R., Mendel, J. T., & Scudder, J. M. 2011, *MNRAS*, 418, 2043
- Elyiv, A., Clerc, N., Plionis, M., et al. 2012, *A&A*, 537, A131
- Fassbender, R., Šuhada, R., & Nastasi, A. 2012, *Advances in Astronomy*, 2012
- Finoguenov, A., Reiprich, T. H., Bohringer, H. 2001, *A&A*, 368, 749
- Finoguenov, A., Briel, U. G., Henry, J. P., Gavazzi, G., Iglesias-Paramo, J., & Boselli, A. 2004, *A&A*, 419, 47
- Gehrels, N. 1986, *ApJ*, 303, 336
- Gerke, B. F., Newman, J. A., Faber, S. M., et al. 2007, *MNRAS*, 376, 1425
- Gilmour, R., Best, P., & Almaini, O. 2009, *MNRAS*, 392, 1509
- Giovanardi, C., Helou, G., Salpeter, E. E., & Krumm, N. 1983, *ApJ*, 267, 35
- Giovanelli, R., & Haynes, M. P. 1985, *ApJ*, 292, 404
- Gisler, G. R. 1978, *MNRAS*, 183, 633
- Gunn, J. E., & Gott, J. R., III 1972, *ApJ*, 176, 1
- Haines, C. P., Pereira, M. J., Sanderson, A. J. R., et al. 2012, *ApJ*, 754, 97
- Haggard, D., Green, P. J., Anderson, S. F., et al. 2010, *ApJ*, 723, 1447
- Hart, Q. N., Stocke, J. T., & Hallman, E. J. 2009, *ApJ*, 705, 854
- Hlavacek-Larrondo, J., Fabian, A. C., Edge, A. C., et al. 2013, *MNRAS*, 431, 1638
- Hopkins, P. F., Hernquist, L., Cox, T. J., et al. 2006, *ApJS*, 163, 1
- Hopkins, P. F., & Hernquist, L. 2006, *ApJS*, 166, 1
- Hopkins, P. F., & Quataert, E. 2011, *MNRAS*, 415, 1027
- Johnson, O., Best, P. N., & Almaini, O. 2003, *MNRAS*, 343, 924
- Kauffmann, G., White, S. D. M., Heckman, T. M., et al. 2004, *MNRAS*, 353, 713
- Kawakatu, N., Anabuki, N., Nagao, T., Umemura, M., & Nakagawa, T. 2006, *ApJ*, 637, 104
- King, I. 1962, *AJ*, 67, 471
- Kocevski, D. D., Faber, S. M., Mozena, M., et al. 2012, *ApJ*, 744, 148
- Koulouridis, E., Plionis, M., Chavushyan, V., et al. 2013, *A&A*, 552, A135
- Koulouridis, E., & Plionis, M. 2010, *ApJ*, 714, L181
- Koulouridis, E., Plionis, M., Chavushyan, V., et al. 2006, *ApJ*, 639, 37
- Koulouridis, E., Chavushyan, V., Plionis, M., Krongold, Y., & Dultzin-Hacyan, D. 2006, *ApJ*, 651, 93
- Larson, R. B., Tinsley, B. M., & Caldwell, C. N. 1980, *ApJ*, 237, 692
- Martini, P., Kelson, D. D., Mulchaey, J. S., & Trager, S. C. 2002, *ApJ*, 576, L109
- Martini, P., Kelson, D. D., Kim, E., Mulchaey, J. S., & Athey, A. A. 2006, *ApJ*, 644, 116
- Martini, P., Mulchaey, J. S., & Kelson, D. D. 2007, *ApJ*, 664, 761
- Martini, P., Miller, E. D., Brodwin, M., et al. 2013, *ApJ*, 768, 1
- Melnyk, O., Plionis, M., Elyiv, A., et al. 2013, *A&A*, 557, A81
- Miller, C. J., Nichol, R. C., Gómez, P. L., Hopkins, A. M., & Bernardi, M. 2003, *ApJ*, 597, 142
- Molnar, S. M., Hughes, J. P., Donahue, M., & Joy, M. 2002, *ApJ*, 573, L91
- Natarajan, P., Kneib, J.-P., & Smail, I. 2002, *ApJ*, 580, L11
- Osterbrock, D. E. 1960, *ApJ*, 132, 325
- Pacaud, F., Pierre, M., Refregier, A., et al. 2006, *MNRAS*, 372, 578
- Pacaud, F., Pierre, M., Adami, C., et al. 2007, *MNRAS*, 382, 1289
- Pierre, M., Pacaud, F., Duc, P.-A., et al. 2006, *MNRAS*, 372, 591
- Popesso, P., & Biviano, A. 2006, *A&A*, 460, L23
- Popesso, P., Biviano, A., Rodighiero, G., et al. 2012, *A&A*, 537, A58
- Pimblett, K. A., Shabala, S. S., Haines, C. P., Fraser-McKelvie, A., & Floyd, D. J. E. 2013, *MNRAS*, 429, 1827
- Sanders, D. B., Soifer, B. T., Elias, J. H., et al. 1988, *ApJ*, 325, 74
- Schlegel, D. J., Finkbeiner, D. P., & Davis, M. 1998, *ApJ*, 500, 525
- Shen, Y., Mulchaey, J. S., Raychaudhury, S., Rasmussen, J., & Ponman, T. J. 2007, *ApJ*, 654, L115
- Silverman, J. D., Kampczyk, P., Jahnke, K., et al. 2011, *ApJ*, 743, 2
- Tanaka, M., Goto, T., Okamura, S., Shimasaku, K., & Brinkmann, J. 2004, *AJ*, 128, 2677
- Umemura, M., Fukue, J., & Mineshige, S. 1998, *MNRAS*, 299, 1123
- van den Bosch, F. C., Aquino, D., Yang, X., et al. 2008, *MNRAS*, 387, 79
- Villforth, C., Sarajedini, V., & Koekemoer, A. 2012, *MNRAS*, 426, 360
- Wen, Z.-L., Yang, Y.-B., Zhou, X., Yuan, Q.-R., & Ma, J. 2006, *Chinese Journal of Astronomy and Astrophysics*, 6, 521
- Wetzel, A. R., Tinker, J. L., & Conroy, C. 2012, *MNRAS*, 424, 232
- Willis, J. P., Pacaud, F., & Pierre, M. 2006, *arXiv:astro-ph/0610800*

Table 1. Low-redshift sample

name (1)	z (2)	kT (3)	L_x, bol (4)	r_{500} (5)	AGN- L_x (6)	Δ_x (7)	Δ_o (8)	δ_x (9)	δ_o (10)	N_x (11)	N_{x1} (12)	N_{x2} (13)	N_{x3} (14)	N_{x4} (15)	N_{x1} (16)	N_{x2} (17)	N_{x3} (18)	N_{x4} (19)	no-z (20)	ABC (21)	
											Projected sources				Cluster members						
XLSSC 041	0.140	1.6	2.74e+43	509	1.0e+42	2.444	0.410	0.405	0.047	7	1(1)	1(1)	2(2)	2(2)	-	1	-	-	-	-	
XLSSC 050	0.140	3.3	9.19e+43	769	1.0e+42	0.878	-	0.896	-	17	1	[3]	[8](5)	[4](2)	-	-	-	-	-	1	x
XLSSC 057	0.155	2.0	3.07e+43	570	1.0e+42	0.431	0.438	-0.560	0.423	4	1	1(1)	-	2	-	-	-	-	-	-	
XLSSC 077	0.200	1.6	1.20e+43	469	1.0e+42	0.396	-	-0.787	-	3	-	1	-	-	-	-	-	-	-	2	x
XLSSC 039	0.231	1.0	6.22e+42	349	1.0e+42	0.029	-	-0.057	-	4	-	-	-	-	-	-	-	-	-	4	x
XLSSC 061	0.257	1.8	2.84e+43	499	1.0e+42	1.687	0.107	1.192	0.092	22	1	5(1)	8(2)	8	-	-	-	-	-	-	
XLSSC 044	0.262	1.2	1.05e+43	388	1.0e+42	-0.295	1.119	0.301	0.262	7	1(1)	-	1(1)	2(1)	-	-	-	-	-	3	
XLSSC 025	0.266	2.1	4.94e+43	541	1.0e+42	0.422	0.277	0.538	-0.030	18	1	2(1)	8(3)	5(2)	1(1)	-	-	-	-	1	
XLSSC 051	0.279	1.4	7.02e+42	418	1.0e+42	0.131	-	0.926	-	13	-	1	-	[2](1)	-	-	-	-	-	10	x
XLSSC 022	0.293	2.0	6.59e+43	514	1.0e+42	-0.308	0.153	0.731	0.133	18	1	1	4(1)	11(5)	-	-	-	-	-	1	
XLSSC 028	0.296	1.2	1.00e+43	369	1.0e+42	-1.000	-	-0.369	-	3	-	-	-	[2](1)	-	-	[1]	-	-	-	x
XLSSC 008	0.299	1.3	1.09e+43	392	1.0e+42	-0.404	0.965	0.291	0.250	8	-	1	1(1)	5(2)	-	-	-	-	-	1	
XLSSC 013	0.307	1.2	1.44e+43	367	1.0e+42	2.863	0.375	0.812	0.026	15	2(2)	4(3)	1	6(4)	-	-	-	-	-	2	
XLSSC 040	0.320	3.9	2.02e+43	775	1.0e+42	-0.153	0.076	0.484	0.266	40	1(1)	3(1)	14(6)	17(8)	-	1	-	-	-	4	
XLSSC 018	0.324	1.5	1.21e+43	424	1.0e+42	-0.552	0.094	0.247	0.101	10	-	1(1)	5(1)	3	-	-	-	-	-	1	
XLSSC 010	0.331	2.5	5.29e+43	581	1.0e+42	0.731	-	0.817	-	30	[2]	[1]	2	[2](1)	-	-	-	-	-	23	x
XLSSC 023	0.328	1.9	3.63e+43	496	1.0e+42	-0.003	-	0.357	-	16	-	[2]	[4](1)	[6](2)	-	-	[1]	-	-	3	x
XLSSC 058	0.333	2.4	1.63e+43	564	1.0e+42	0.244	0.183	0.089	-0.183	19	1	3(2)	6(3)	7(2)	-	-	-	-	-	2	
XLSSC 056	0.350	3.5	1.24e+44	722	1.1e+42	0.535	0.396	-0.381	0.288	20	-	6(1)	6	4(1)	-	-	-	1	-	3	

Notes. (1) original name in the XMM-LSS database, (2), redshift, (3) cluster's temperature in keV, (4) cluster's luminosity in erg s^{-1} , (5) r_{500} in Mpc, (6) point source's lower X-ray luminosity limit in erg s^{-1} in the [0.5-2] keV band, (7) X-ray point source overdensity up to $2r_{500}$, (8) optical galaxy overdensity up to $2r_{500}$, (9) X-ray point source overdensity from 2 to $4r_{500}$, (10) optical galaxy overdensity from 2 to $4r_{500}$, (11) total number of X-ray sources up to $4r_{500}$, (12)-(15) number of projected X-ray sources in annuli 1 to 4, respectively; the parentheses denote the spectroscopically confirmed sources, (16)-(19) as for (12)-(15) but for true cluster members (projected sources and cluster members are disjoint), (20) sources with no redshift, (21) when marked the clusters are located in the CFHT ABC fields (see Fig. 1), where redshifts were calculated using only 4-6 photometry bands. Numbers in brackets denote sources in the ABC supplementary fields.

Table 2. High-redshift sample

name (1)	z (2)	kT (3)	$L_{x,bol}$ (4)	r_{500} (5)	AGN- L_x (6)	Δ_x (7)	Δ_o (8)	δ_x (9)	δ_o (10)	N_x (11)	N_{x1} (12)	N_{x2} (13)	N_{x3} (14)	N_{x4} (15)	N_{x5} (16)	N_{x1} (17)	N_{x2} (18)	N_{x3} (19)	N_{x4} (20)	N_{x5} (21)	no-z (22)	ABC (23)
											Projected sources					Cluster members						
XLSSC 006	0.429	5.6	6.70e44	0.924	1.7e42	-0.019	-	0.175	-	55	[2]	[4]	[10](2)	[18](2)	[13](2)	-	-	-	-	[1]	7	x
XLSSC 036	0.494	3.8	3.01e44	0.694	2.4e42	1.501	-	0.511	-	45	[1]	[8](1)	[7]	[11](2)	[7]	-	-	[1]	-	[1]	9	x
XLSSC 053	0.494	3.5	3.26e44	0.498	2.4e42	0.539	0.393	0.567	0.106	20	-	2	4(2)	3	6(2)	-	1	-	-	1	3	
XLSSC 049	0.496	2.9	5.02e43	0.583	2.4e42	0.395	0.143	0.562	-0.039	27	-	3(3)	3(3)	8(3)	7(3)	-	-	1	1	-	4	
XLSSC 001	0.614	3.3	3.57e44	0.591	4.0e42	-0.585	0.118	0.105	-0.046	12	-	1	-	1	-	-	-	-	-	2	8	
XLSSC 059	0.645	2.7	6.20e43	0.564	4.5e42	0.046	0.078	-0.135	0.197	10	1	-	1(1)	1(1)	3(2)	-	-	-	-	1	3	
XLSSC 080	0.646	1.5	3.41e43	0.352	4.5e42	1.517	0.102	-0.677	0.004	5	1(1)	-	3(2)	-	1	-	-	-	-	-	-	
XLSSC 076	0.752	1.3	9.63e43	0.298	6.4e42	-0.070	0.558	0.493	0.298	4	-	-	1	2	-	-	-	-	-	-	1	
XLSSC 002	0.772	2.6	1.83e44	0.467	6.7e42	-0.236	0.247	0.439	0.022	9	-	1	-	2	2(2)	-	1	-	-	1	2	
XLSSC 003	0.835	3.2	3.34e44	0.509	8.2e42	-0.632	-	1.326	-	13	-	-	[1]	[2]	[3]	-	-	-	[3]	[1]	3	x
XLSSC 078	0.960	3.3	1.32e44	0.479	1.1e43	-0.182	0.114	0.114	0.083	7	-	1(1)	1(1)	2	3(1)	-	-	-	-	-	-	
XLSSC 072	1.003	3.5	5.28e44	0.485	1.3e43	1.766	-	0.671	-	13	[1]	[2]	-	[2]	[1]	-	[2]	-	[1]	[1]	3	x
XLSSC 048	1.005	3.0	1.61e44	0.439	1.3e43	-0.440	-	0.459	-	6	-	-	[1]	-	[1]	-	-	-	-	[2]	2	x
XLSSC 005	1.053	2.7	1.38e44	0.400	1.4e43	0.789	-	0.300	-	7	-	2	-	[2](1)	[1]	-	[1]	-	-	[1]	-	x

Notes. (1) original name in the XMM-LSS database, (2), redshift, (3) cluster's temperature in keV, (4) cluster's luminosity in erg s⁻¹, (5) r_{500} in Mpc, (6) point source's lower X-ray luminosity limit in erg s⁻¹ in the [0.5-2] keV band, (7) X-ray point source overdensity up to $3r_{500}$, (8) optical galaxy overdensity up to $3r_{500}$, (9) X-ray point source overdensity from 3 to $5r_{500}$, (10) optical galaxy overdensity from 3 to $5r_{500}$, (11) total number of X-ray sources up to $5r_{500}$, (12)-(16) number of projected X-ray sources, in annuli 1 to 5, respectively; the parentheses denote the spectroscopically confirmed sources, (16)-(20) as for (12)-(16) but for true cluster members (projected sources and cluster members are disjoint), (22) sources with no redshift, (23) when marked the clusters are located in the CFHT ABC fields (see Fig. 1), where redshifts were calculated using only 4-6 photometry bands.

Numbers in brackets denote sources in the ABC supplementary fields.

The cluster XLSSC 078, although covered by CFHTLS, is excluded from the optical stacking analysis because $m_i^* + 1 > 24$.